Earthquake Engineering & Structural Dynamics

WILEY

RESEARCH ARTICLE OPEN ACCESS

Finite Element Modelling of Rocking and Hybrid Precast Walls under Seismic Loading

Andrea Belleri[1] | Michele E. Bressanelli[1] | Simone Labò[1] | Jose I. Restrepo[2]

[1]Department of Engineering and Applied Sciences, University of Bergamo, Dalmine, Italy | [2]Head of R&D, Nabih Youssef Associates, Los Angeles, California, USA

Correspondence: Andrea Belleri (andrea.belleri@unibg.it)

Received: 15 May 2025 | **Revised:** 21 March 2026 | **Accepted:** 24 March 2026

Keywords: hybrid wall | numerical optimisation | precast structures | self-centring systems | rocking wall

ABSTRACT

In recent years, self-centring systems have received considerable research interest in the seismic design of precast concrete structures for their ability to limit damage and satisfy resilience requirements. Rocking and hybrid structural walls, characterised by the formation of a single gap at the wall–foundation interface, mitigate damage by permitting controlled rocking motion, while gravity loads and unbonded post-tensioning tendons provide the restoring force necessary for self-centring. Supplementary energy dissipation is typically supplied by partially unbonded mild steel bars, producing the characteristic flag-shaped hysteretic response. This study examines the finite element modelling of rocking and hybrid precast concrete walls, with particular focus on the influence of key modelling assumptions and parameters governing the wall–foundation interface. Both component-level (single-wall) and system-level (full-structure) models are considered. Three alternative modelling strategies are evaluated to represent the rocking interface: (i) fibre-based beam elements, (ii) distributed compression-only translational springs and (iii) lumped nonlinear rotational springs at the wall base. Nonlinear static and dynamic analyses are conducted, and numerical results are validated against shake-table tests performed on a three-storey, half-scale precast concrete building representative of a parking structure, tested on the Large High-Performance Outdoor Shake Table at the University of California, San Diego. To enable consistent interpretation of the modelling results and to account for the coupled influence of multiple parameters on the nonlinear response, a constrained nonlinear least-squares optimisation employing a multistart strategy is used to calibrate the numerical models by minimising the discrepancy between experimental and simulated displacement and base shear time histories. The results delineate the relative strengths and limitations of each modelling approach. The proposed wall–foundation rocking interface formulations incorporating either fibre-based beam elements or distributed compression-only translational springs demonstrate very good agreement with the experimental measurements.

1 | Introduction

Re-centring structural systems provide an effective means of reducing seismic vulnerability and minimise or even eliminate building downtime after an earthquake. These systems use unbonded post-tensioning cables or bars sleeved within precast structural elements and often incorporate hysteretic or viscous devices for energy dissipation. They are classified as either rocking systems or hybrid systems, with the latter incorporating hysteretic energy dissipation devices to further improve performance. The main advantages of these systems are limiting structural seismic damage and increasing post-earthquake building operational capacity. Rocking walls, or rocking frames, consist of one or more

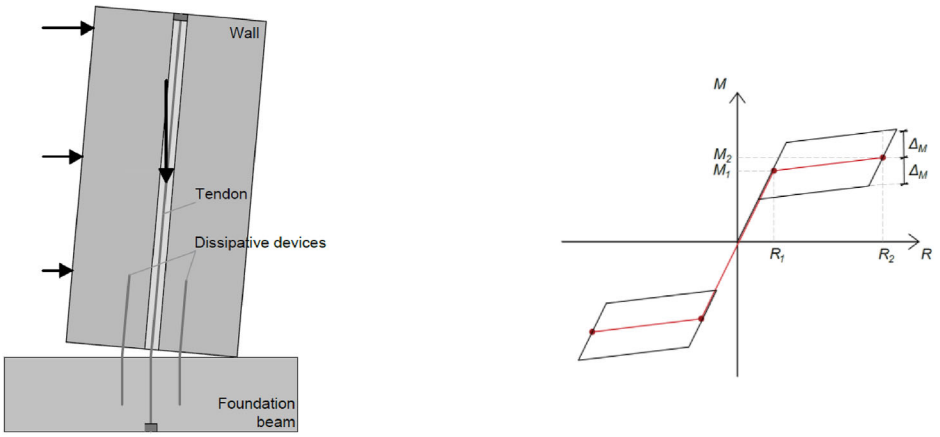

(a) (b)

FIGURE 1 | (a) Schematic view of a rocking-hybrid wall; (b) idealised behaviour for the rocking wall (red line—elastic bilinear) and hybrid wall (black line—flag-shaped) configurations.

framing elements that can rotate ('rock') at specific interfaces [1–13].

To increase the energy dissipation of rocking systems, which otherwise exhibit elastic bilinear behaviour with limited damping, additional dissipation devices may be incorporated [13]; [8, 14–17]; [18], such as unbonded mild steel bars, hysteretic devices, linear or non-linear fluid-viscous devices and friction devices. These systems are defined as 'hybrid' and are characterised by a flag-shaped hysteretic curve (Figure 1).

As part of the PRESSS project, various studies and experimental tests have been conducted on rocking and hybrid systems [6, 19–21], combining precast walls with unbonded mild steel bars at the wall–foundation interface or with external dissipative elements, such as viscous devices. The resulting system exhibits a hysteretic response characterised by the typical flag-shaped curve, in which the yielding of the longitudinal mild steel bars provides the required energy dissipation, with an equivalent viscous damping ratio greater than 28%, according to Holden et al. [8].

This paper examines the finite element modelling of rocking and hybrid walls to assess the impact of different modelling strategies on the global seismic response of rocking systems [6, 22–27]. Three modelling approaches for analysing the nonlinear response of the rocking wall–foundation interface are discussed herein: (i) fibre elements at the wall–foundation interface [22, 28, 29], (ii) multiple compression-only translational springs and (iii) a lumped rotational spring [28, 30, 31].

Single walls were first modelled with nonlinear finite elements to evaluate the effectiveness of the modelling strategies at the component level, where parameters and response quantities can be more easily controlled. Sensitivity analyses were also conducted to assess the influence of key modelling assumptions. The testbed used to compare the various modelling approaches is the three-storey precast building of the Diaphragm Seismic Design Methodology (DSDM) research programme [11, 32, 33]. This building was constructed at half-scale and tested on the US National Science Foundation-funded Large High-Performance Outdoor Shake Table (LHPOST) at the University of California, San Diego [34, 35]. All numerical models were developed using the open-source finite element software OpenSees [36]. An analytical formulation is then derived to capture the concrete deformation at the wall base and define the stiffness of the rocking interface elements. Complete models of the entire building are subsequently developed by incorporating the wall modelling strategies and insights obtained from the single-wall analyses. Finally, a least-squares optimisation procedure is implemented to identify the optimal values of the main parameters governing the nonlinear dynamic response of the building, showing good agreement with those derived from the proposed analytical formulation.

2 | Description of the Testbed Structure

The testbed building was built at half-scale, satisfying geometric-similitude and tested in 2008. The main dimensions of the building are shown in Figure 2. The total height was 7.01 m, and the plan measured 17.1 m long and 4.88 m width. The inter-storey height of each floor was 1.98 m. The floor masses were 208, 219 and 195 kN/g for the first, second, and third floors, respectively. The gravity load was supported by ten precast columns. Two 2.44 m long by 7.01 m high by 0.2 m thick post-tensioned walls provided the bulk of the lateral resistance. Each wall had two sets of post-tensioned tendons (five strands each with an area of 495 mm^2) for re-centring capacity (Figure 2a). The walls were configured as rocking walls for sites in low-seismic regions and as hybrid walls for moderate and high-seismic regions. The change in configuration from rocking to hybrid was achieved by grouting partially unbonded reinforcing steel bars at the wall–foundation interface [7, 11, 37] and by changing the prestressing force. The concrete cylinder compressive strength of the walls was 53 MPa, as average value during the testing period, with an ultimate deformation capacity of 0.55% in unconfined areas, and 81 MPa and 3.8%, respectively, in the confined regions at the wall toes, as obtained according to Mander et al. [38].

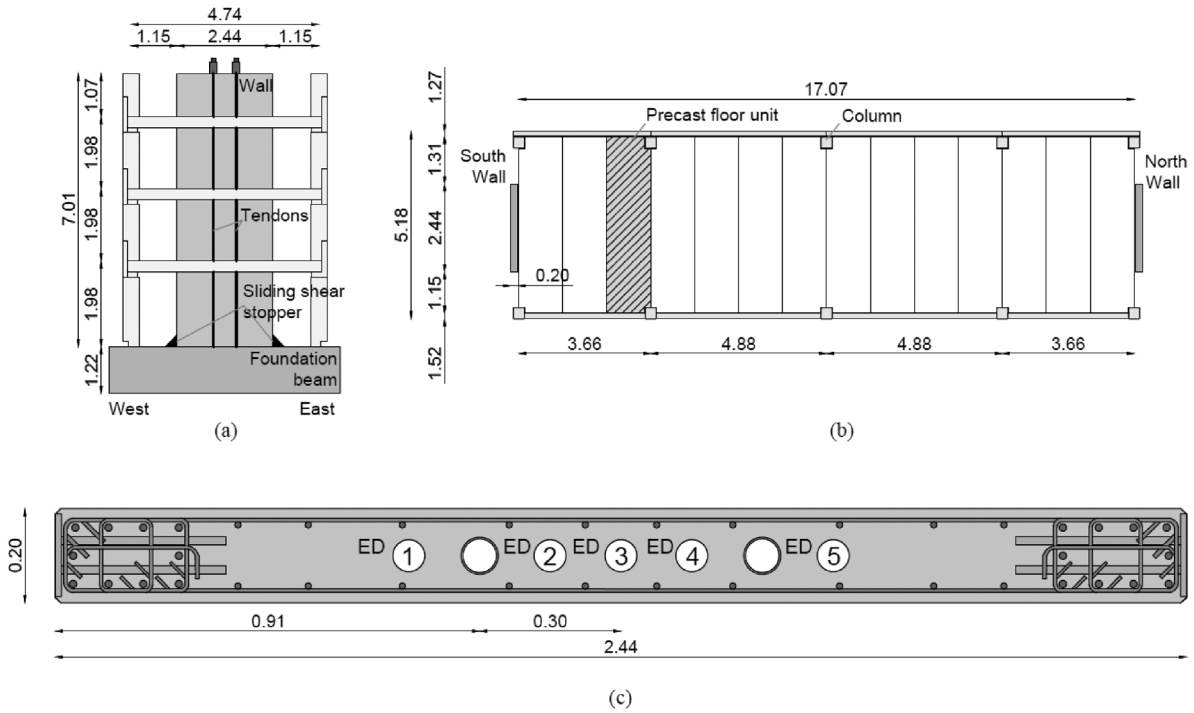

FIGURE 2 | (a) Geometry of the wall, (b) plan view of the building and (c) wall base cross-section. The measurements are expressed in meters.

Walls were prestressed with 5 × 12.7 mm diameter low-relaxation strands meeting ASTM A416. The strands had a measured yield strength, defined by the 0.2% strain offset method, of 1800 MPa and a tensile strength of 1915 MPa. When the walls were configured as 'rocking', each tendon was stressed to 236 kN before testing, whereas for the 'hybrid' configuration, the stressing force in each tendon was increased to 321 kN before testing. The dissipators consisted of 22 mm reinforcing bars meeting ASTM A706. The measured yield and tensile strengths of these bars were 490 and 673 MPa, respectively. The measured uniform elongation was 12.3%. The dissipators were embedded inside a corrugated steel duct placed in the precast wall, but the ducts were only grouted when changing the walls from the rocking to the hybrid configuration. For this purpose, the dissipators in positions 2 and 4 (Figure 2c) were grouted.

The structure was tested using ground motions representative of different seismic regions. The seismic sequences correspond to the cities of Knoxville (Tennessee), Seattle (Washington) and Berkeley (California), which are characteristic of US regions with low, medium and high seismicity, respectively [11]. For the Knoxville case, a rocking wall configuration was used, that is, without grouting the bars at the wall–foundation interface. In contrast, for the Seattle and Berkeley cases, a hybrid wall configuration was considered by grouting the bars as previously mentioned [32]. The Berkeley case was further subdivided into Berkeley-DBE for the design earthquake and Berkeley-MCE for the maximum considered earthquake. Figure 3 presents the unscaled elastic response spectra (5% damping) for each scenario, including the fundamental period of the structure obtained from low-amplitude white-noise excitation [37].

No damage was observed during the Knoxville test, with limited uplifting at the wall base. The Seattle test showed no wall damage but diaphragm chord failures requiring repair; the final test

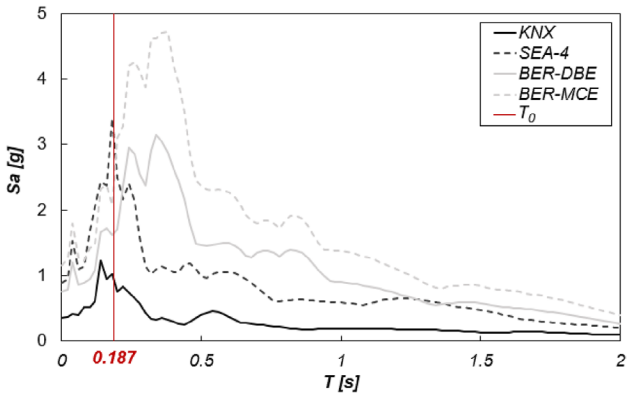

FIGURE 3 | Unscaled pseudo-acceleration response spectra for the test model structure (5% damping).

Note: T_0 is the reference period of the tested structure.

(Seattle-4) is adopted as reference. During the Berkeley-DBE test, a post-tensioning cable broke, affecting the subsequent Berkeley-MCE test [32, 37]. The Knoxville response was essentially elastic nonlinear, with a maximum base rotation of 3.2 mrad. The Seattle and Berkeley tests exhibited hybrid behaviour with flag-shaped hysteresis, reaching maximum base rotations of 8.7 and 19.2 mrad, respectively. In all cases, damage was limited to minor concrete spalling at the wall base. Detailed results can be found in Schoettler et al. [11] and Belleri et al. [32].

3 | Finite Element Modelling: Single Wall

Three alternative modelling strategies are investigated to represent the nonlinear rocking behaviour at the wall–foundation interface: a fibre-based formulation, a multiple compression-only

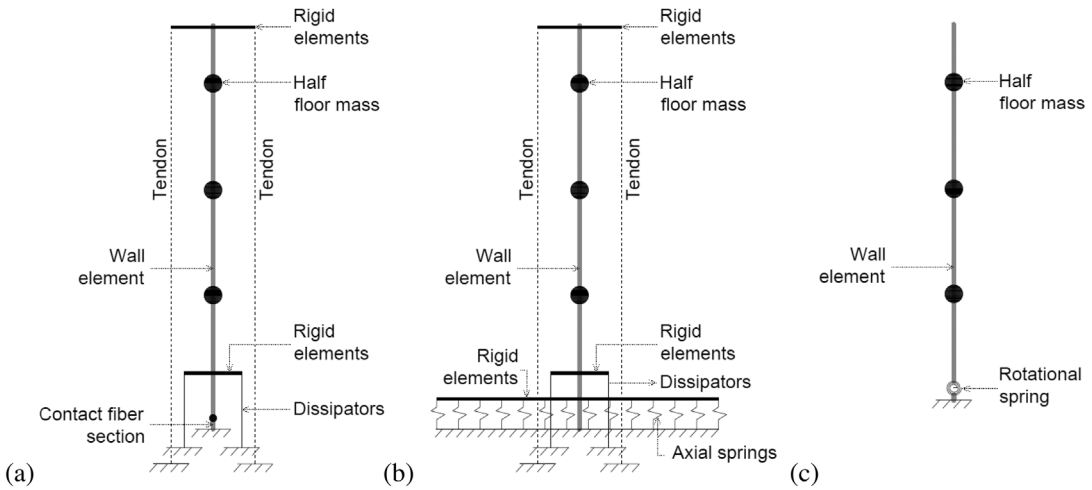

FIGURE 4 | Representation of the considered FE models: (a) fibre model, FM; (b) multiple compression-only translational spring model, MS; (c) rotational lumped spring, RS.

TABLE 1 | Starting values of the parameters considered in the sensitivity analysis.

Parameter	FM	MS
L_s	$6\phi_d + 6\phi_d$	$6\phi_d + 6\phi_d$
$E_{rocking}$	$0.02{\cdot}E_c$	//
N_x	125	//
L_{spring}	//	$0.5{\cdot}L_{wall}$
ξ	0.01	0.01

translational spring model, and a lumped nonlinear rotational spring model. The modelling strategy is developed in two stages. First, finite element models of a single wall (Figure 4) are used to evaluate the influence of key modelling parameters governing rocking under controlled conditions. Subsequently, the wall models are implemented in the finite element model of the complete structure to evaluate the system-level response. All numerical models were developed using the open-source software OpenSees [36]. In the single-wall models, lumped masses were assigned at each floor level, and fibre elements were used to model the wall. Because diaphragm masses dominate the total mass, the rotational inertia of the walls is neglected. The effectiveness of the three finite element modelling approaches was then systematically evaluated by comparing their ability to reproduce the experimentally observed response at both the component and structural system levels.

In the rotational-spring (RS) formulation, the rocking behaviour is fully captured by introducing a nonlinear rotational spring that connects the base of the wall to the ground. The rotational spring is implemented using a *ZeroLength* element with a multilinear hysteretic law, following the classical formulation proposed by Vulcano and Bertero [39]. The nonlinear properties of the rotational spring are defined according to the analytical expressions proposed by Restrepo and Rahman [7], adopting a bilinear elastic idealisation to reproduce the characteristic moment-rotation response associated with rocking behaviour [22]. For the hybrid wall configurations, an additional rotational spring is placed in parallel with the rocking spring to represent the energy-dissipating devices' contribution. This component is modelled using the Dodd-Restrepo hysteretic formulation [40], allowing consistent representation of the nonlinear behaviour of the grouted reinforcing bars [24, 41].

In the multi-spring (MS) formulation, the wall-foundation interface is represented by a series of axial springs acting only in compression [42, 43], allowing separation between the wall and the foundation during rocking. The distributed contact behaviour at the interface is approximated by uniformly placing 25 elasto-plastic compression-only springs along the base of the wall. The elastic stiffness of each spring is defined as $k_{spring} = E_c\ A/L_{\text{spring}}$, where E_c is the modulus of elasticity of the wall concrete, A is the tributary area associated with each spring, and L_{spring} is a reference length. This parameter represents an equivalent compression zone at the base of the wall and was provisionally assumed equal to half of the wall length L_w, in accordance with previous studies [19, 43, 44]. Its influence is investigated in the next section.

In the fibre-based formulation (FM), the rocking behaviour is represented by a fibre section at the wall–foundation interface without reinforcing bars and with no tensile strength in the concrete. This region was modelled using *dispBeamColumn* elements with fibre sections assigned an elastic no-tension (ENT-type) uniaxial material. The elastic properties of the interface were defined to ensure consistency with the axial stiffness used in the MS model: considering a contact element with a thickness s = 25 mm, the resulting elastic modulus of the fibre element at the wall–foundation interface is $E_{rocking} = 0.02\ E_c$.

$$k_{spring} = k_{contact\ element} \rightarrow \frac{E_c A}{L_w/2} = \frac{E_{rocking} A}{s}$$

$$\rightarrow E_{rocking} \approx 0.02 E_c \quad (1)$$

Within the fibre cross-sections of the wall, confined reinforced concrete was modelled using the *Concrete07* uniaxial material

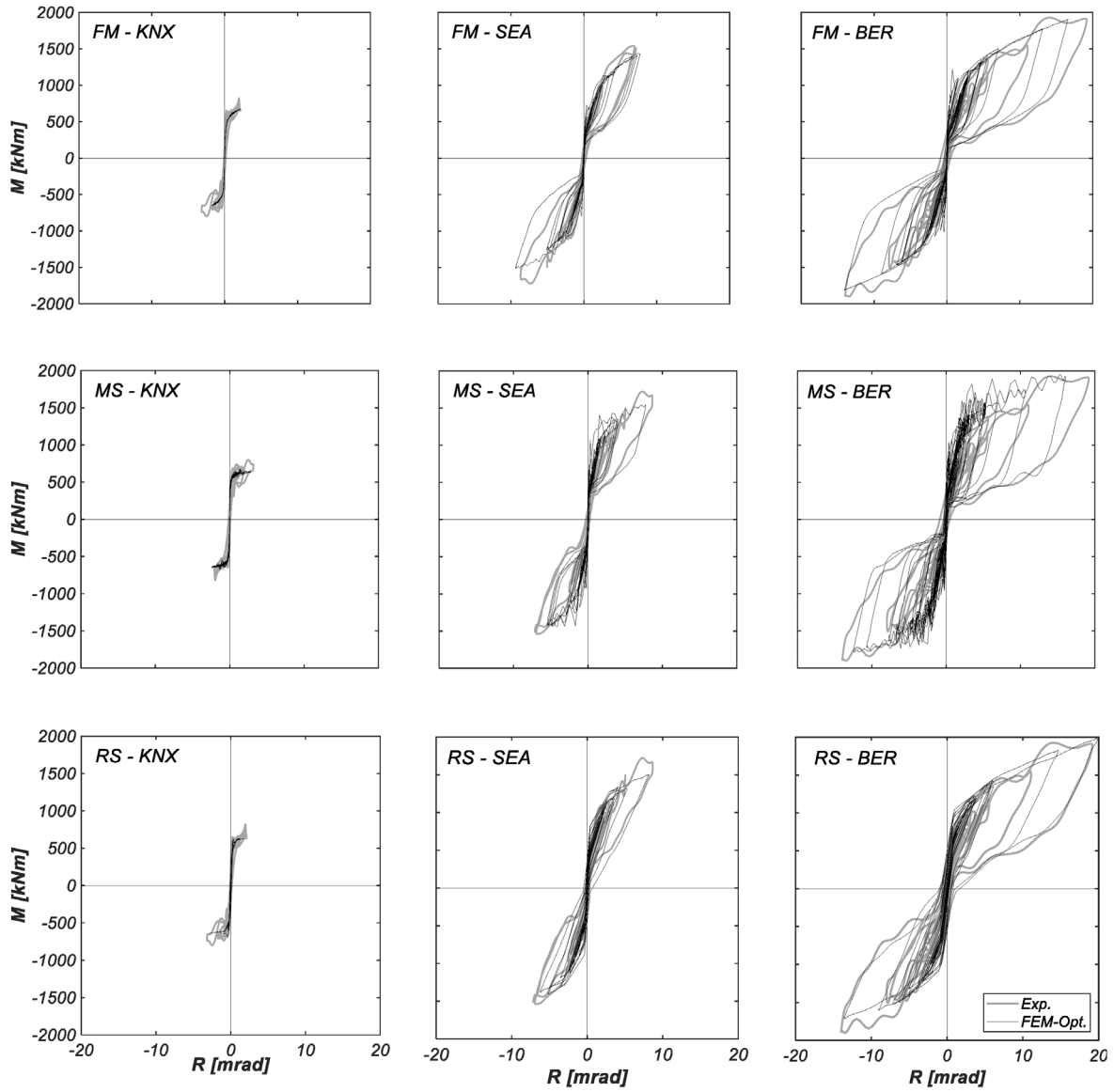

FIGURE 5 | Moment-rotation diagrams for FM, MS and RS models for the Knoxville, Seattle-4 and Berkeley-DBE tests.

Note: In the grey line is the experimental test and in the black line the numerical results.

based on the formulation proposed by [38], allowing a realistic representation of nonlinear compressive behaviour in the wall toe region.

In both the fibre-based and MS formulations, each post-tensioning tendon is modelled using a truss element, pinned at the base and rigidly connected to the top of the wall via rigid links. The energy-dissipating devices are also represented by truss elements, whose nonlinear cyclic behaviour is described using the Dodd–Restrepo hysteretic model [40], with the Bauschinger effect Omega factor set to 0.75. The effective length of the dissipators corresponds to the unbonded length provided at the wall–foundation interface (38 mm), achieved by wrapping the bars with adhesive tape, plus an additional length on each side to account for strain penetration. Assuming a strain penetration length equal to six bar diameters per side, the total effective length is $L_s = 132$ mm [29, 32]. This assumption corresponds to a triangular strain distribution over approximately 12 bar diameters, equivalent to a constant strain over six diameters per side.

When developing the numerical models for the nonlinear time-history analyses, particular attention was devoted to the selection of an appropriate damping formulation [45–47]. The most common representation of damping is Rayleigh damping, in which the viscous damping matrix is obtained as a linear combination of the mass ($\mathbb{M}$) and stiffness ($\mathbb{K}$) matrices.

$$C = \alpha\, \mathbb{K} + \beta\, \mathbb{M} \tag{2}$$

For rocking systems, this formulation may generate spurious viscous forces at the wall–foundation interface when the initial stiffness matrix is used, particularly during phases when the gap between the wall and the foundation opens [22]. In these conditions, relative velocities at the interface induce fictitious damping forces in both FM and MS models. An apparent appeal-

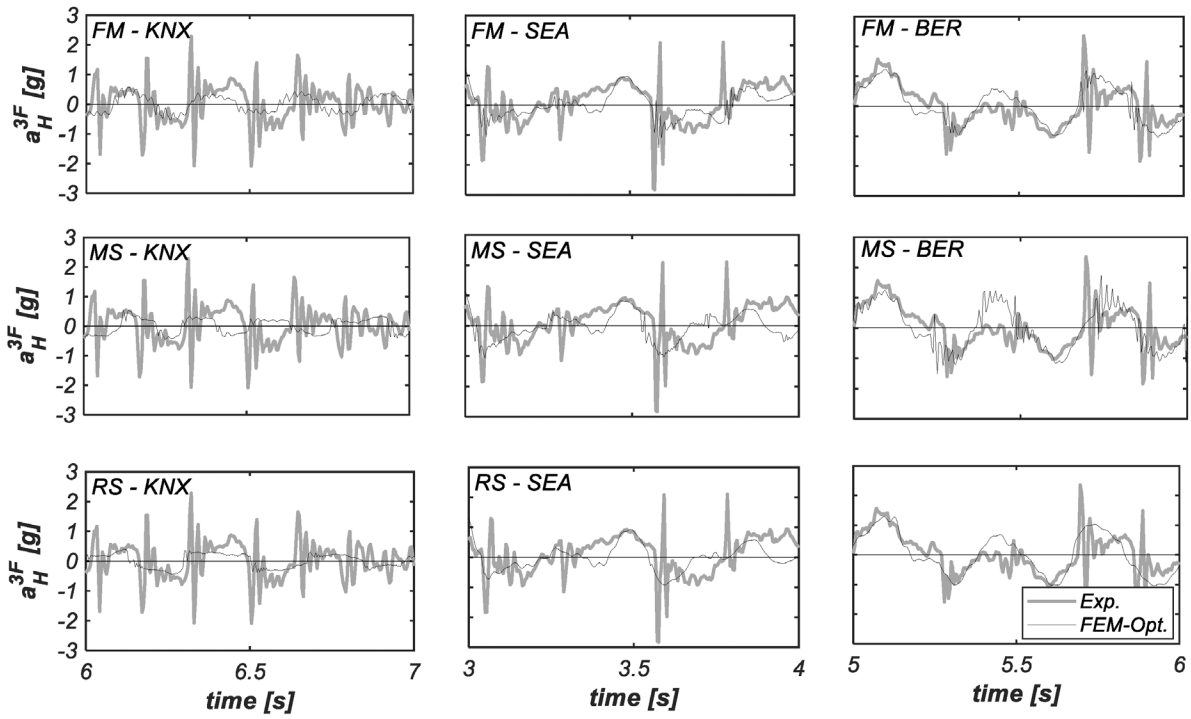

FIGURE 6 | Horizontal acceleration time history at the third floor for the FM, MS and RS model for Knoxville, Seattle-4 and Berkeley-DBE.

Note: In the grey line is the experimental test and in the black line the numerical results.

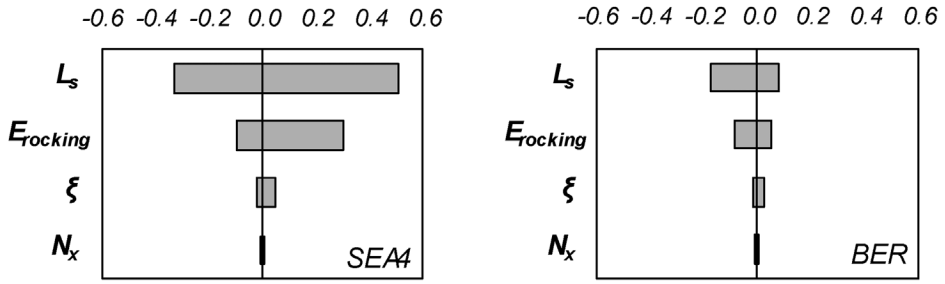

FIGURE 7 | Tornado diagram showing the sensitivity of several parameters in the FM model for Seattle-4 and Berkeley ground motion. Results expressed as percentage variation in the maximum displacement at the third floor.

ing alternative is to use a tangent-stiffness-proportional damping formulation. However, this approach becomes problematic when stiffness softening or negative tangent stiffness occurs, as it produces negative damping forces that spuriously inject energy into the system. This issue is especially relevant due to the load peaks and negative-stiffness response during gap closure [32].

Radiation damping [48, 49] is often considered in soil–structure interaction problems involving rocking bodies, as it arises from relative displacements between the foundation and the surrounding free field. However, its contribution decreases significantly under non-radiating boundary conditions, where material and interface-related dissipation mechanisms predominate [50, 51]. In the present experimental configuration, the rocking walls are supported by a stiff post-tensioned RC foundation beam resting on low-friction sliding bearings, rather than on a soil half-space. Accordingly, radiation damping is neglected. Energy dissipation associated with material deformation is captured through the nonlinear wall formulations, while additional dissipation not explicitly modelled is represented through a small mass-proportional viscous damping ratio (1%). This term provides a numerically stable equivalent representation of friction, gap-closure effects and secondary dissipation mechanisms.

Non-linear dynamic analyses were conducted considering the actual sequence of ground motions used during the experimental tests. Figure 5 presents the results of the three FE models in terms of base moment (M) as a function of base rotation (R), demonstrating that the models can adequately describe the global wall behaviour.

Figure 6 shows the horizontal accelerations at the top floor, which exhibits the largest amplification and most pronounced spikes. These spikes are associated with the temporary increase in lateral stiffness during unloading near zero rotation [32, 52]. The FE models reproduce the overall trend but underestimate these peaks. Overall, the results show that the single wall models accurately predict the moment–rotation response,

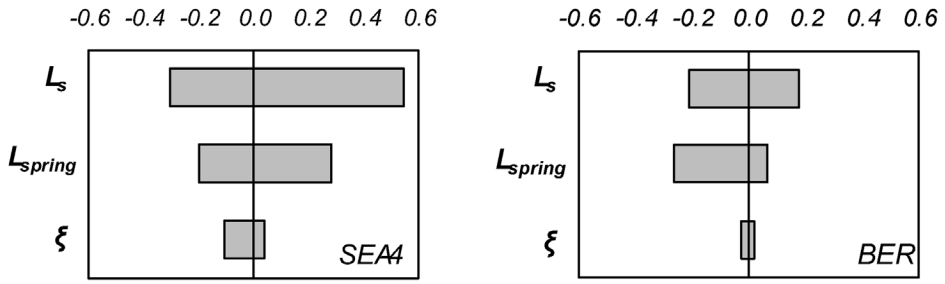

FIGURE 8 | Tornado diagram showing the sensitivity of several parameters in the MS model for Seattle-4 and Berkeley ground motion. Results expressed as percentage variation in the maximum displacement at the third floor.

although differences arise during gap closure due to acceleration spikes.

A sensitivity analysis was conducted to assess the influence of the modelling parameters on the wall's response. Each parameter was doubled and halved with respect to its reference value. The parameters considered are: the strain penetration length (L_s) for the hysteretic devices (the reference value is six times the diameter, ϕ_d, of the dissipation bar for each side of the rocking interface); the modulus of elasticity of the element at the rocking interface ($E_{rocking}$); the number of fibre subdivisions (N_x) along the longitudinal direction at the rocking interface; the reference length of the translational compression-only springs at the wall base (L_{spring}); the damping ratio used in the analyses (ξ). The initial values for each parameter are given in Table 1 for the FM and MS models.

Figure 7 shows the influence of the most important parameters of the FM model on the maximum displacement of the wall on the third floor. The results are presented in a tornado diagram, considering the ground motions of Seattle and Berkeley. L_s is the most significant parameter affecting the FM model results followed by $E_{rocking}$, while N_x and ξ have limited influence.

Similarly, Figure 8 shows the influence of the MS model parameters. The response is mainly governed by L_s and L_{spring}. A sensitivity analysis on the number of springs confirms that 25 springs are adequate for global response prediction [22, 28, 43], while a higher discretisation is required for local contact behaviour.

4 | Rocking Interface Stiffness Model

Given the dominant role of the rocking interface deformability highlighted by the sensitivity analyses, as represented by L_{spring} in the MS formulation and by E_{rocking} in the fibre-based model, an analytical evaluation of the compressive strain development at the wall base is performed. During rocking, a stress discontinuity region develops at the wall-foundation interface, within which compressive stresses are concentrated. This region is assumed to extend over a characteristic height of the order of the wall length L_w. Under this assumption, the depth of the compressed zone may be idealised as varying linearly from the neutral axis at the wall base to the full wall width at a height equal to L_w (Figure 9a). A triangular strain distribution is assumed for each cross-section within this region (Figure 9a).

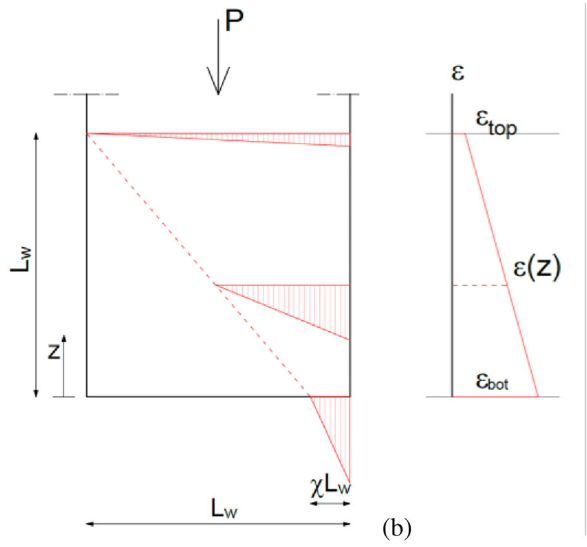

FIGURE 9 | (a) Idealised strain distribution at the bottom of the wall during rocking. (b) Corresponding strain distribution at the outer compressed edge of the wall during rocking.

TABLE 2 | $E_{rocking}$ and L_{spring} obtained for different neutral axis ratios.

χ	$E_{Rocking}$	L_{spring}
0.10	0.0155 E_c	0.66 L_w
0.15	0.0148 $\mathbf{E_c}$	0.69 $\mathbf{L_w}$
0.20	0.0142 E_c	0.72 L_w
0.30	0.0131 E_c	0.78 L_w

The shortening of the outer compressed edge can be calculated by integrating the axial deformations along the wall height in the discontinuity region (Figure 9b). The bottom and top compressive strains in this region are:

$$\begin{cases} \varepsilon_{bot} = \frac{2P}{\chi \cdot L_w \cdot t} \cdot \frac{1}{E_c} \\ \varepsilon_{top} = \frac{2P}{L_w \cdot t} \cdot \frac{1}{E_c} \end{cases} \tag{3}$$

where P is the axial load resulting from gravity and post-tension, χL_w is the neutral axis depth, t is the wall thickness and E_c is the concrete elastic modulus.

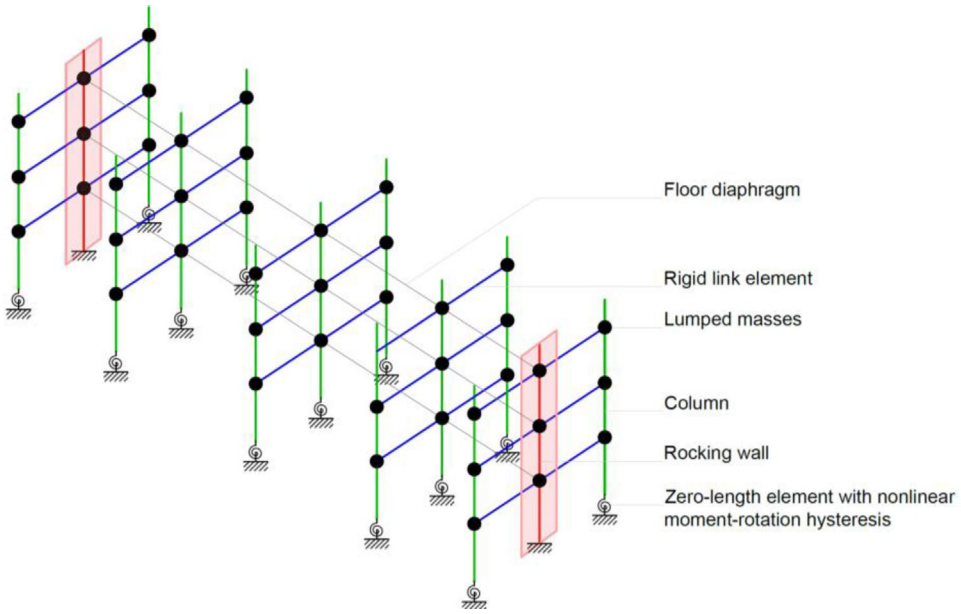

FIGURE 10 | Scheme of the FE model of the entire building.

TABLE 3 | Best parameter values resulting from the optimisation process (FM and MS models).

	FM model			MS model		
	$E_{rocking}$	ξ	L_s	K_{spring}	ξ	L_s
KNX	$0.0152 \cdot E_c$	0.2%	//	$1.60 \cdot K_{spring}$	0.5%	//
SEA-4	$0.0152 \cdot E_c$	0.5%	$12\,\phi_d$	$0.48 \cdot K_{spring}$	2.0%	$6\,\phi_d$
BER	$0.0152 \cdot E_c$	0.5%	$12\,\phi_d$	$0.80 \cdot K_{spring}$	2.0%	$6\,\phi_d$
Ref. Values	$0.0148 \cdot E_c$	0.5%	$12\,\phi_d$	$1.45 \cdot K_{spring}$	0.5%	$12\,\phi_d$

Assuming a linear strain variation along the height (Figure 9b), the axial shortening at the wall base is:

$$\Delta = \int_0^{L_w} \varepsilon(z)\, dz = \int_0^{L_w} \left[\varepsilon_{bot} + \frac{\varepsilon_{top} - \varepsilon_{bot}}{L_w} z\right] dz = \frac{P}{E_c t} \frac{\chi + 1}{\chi} \quad (4)$$

In the proposed finite element models, this shortening must be reproduced by the stiffness of the interface elements.

An equivalent axial stiffness k_{eq} is derived by considering an effective load footprint at the outermost compressed wall edge. The effective area is assumed equal to one-third of the neutral axis length, that is, $A = \frac{1}{3}\chi L_w t$, and the corresponding portion of the axial load is $F = \frac{5}{9} P$. The equivalent stiffness is therefore:

$$k_{eq} = \frac{F}{\Delta} = \frac{F}{\frac{P}{E_c \cdot t} \cdot \frac{\chi+1}{\chi}} \xrightarrow{A=\frac{1}{3}\chi \cdot L_w \cdot t} k_{eq} = \frac{5}{3} \frac{AE_c}{L_w} \cdot \frac{1}{\chi + 1} \quad (5)$$

By comparison with the classical axial stiffness expression $k = \frac{AE_c}{L_{\text{spring}}}$, the equivalent spring length is:

$$L_{spring} = \frac{3}{5} (\chi + 1) L_w \quad (6)$$

This expression provides a mechanically consistent estimate of L_{spring}, linking the discrete interface representation to the axial deformation mechanism at the wall base.

In the fibre-based formulation, the rocking interface is represented by a compressive layer with equivalent elastic modulus E_{rocking} and thickness $s = 25\,\text{mm}$. By enforcing equivalence between the analytical shortening and the deformation of the interface layer, the following relationship is obtained:

$$\frac{P}{E_c t} \frac{\chi + 1}{\chi} = \frac{5}{3} \frac{P}{\chi L_w t} \frac{s}{E_{rocking}} \rightarrow E_{Rocking} = \frac{5}{3} \frac{1}{\chi + 1} \frac{s \cdot E_c}{L_w} \quad (7)$$

Table 2 summarises the corresponding values of $E_{rocking}$ and L_{spring} for different neutral axis ratios χ.

Based on design assumptions and available experimental evidence [32], a representative value of $\chi \approx 0.15$ is adopted, yielding $L_{spring} \approx 0.69 L_w$ and $E_{rocking} \approx 0.0148 E_c$.

Although simplified, this representation provides a mechanically consistent representation of the axial deformation associated with rocking and supports the definition of equivalent interface parameters. Further details are reported in the Appendix.

5 | Finite Element Modelling: System Level

To validate the analytical formulations underlying the selection of the rocking-related parameters, namely L_{spring}, E_{rocking} and L_s, a comprehensive global analysis of the reference building was

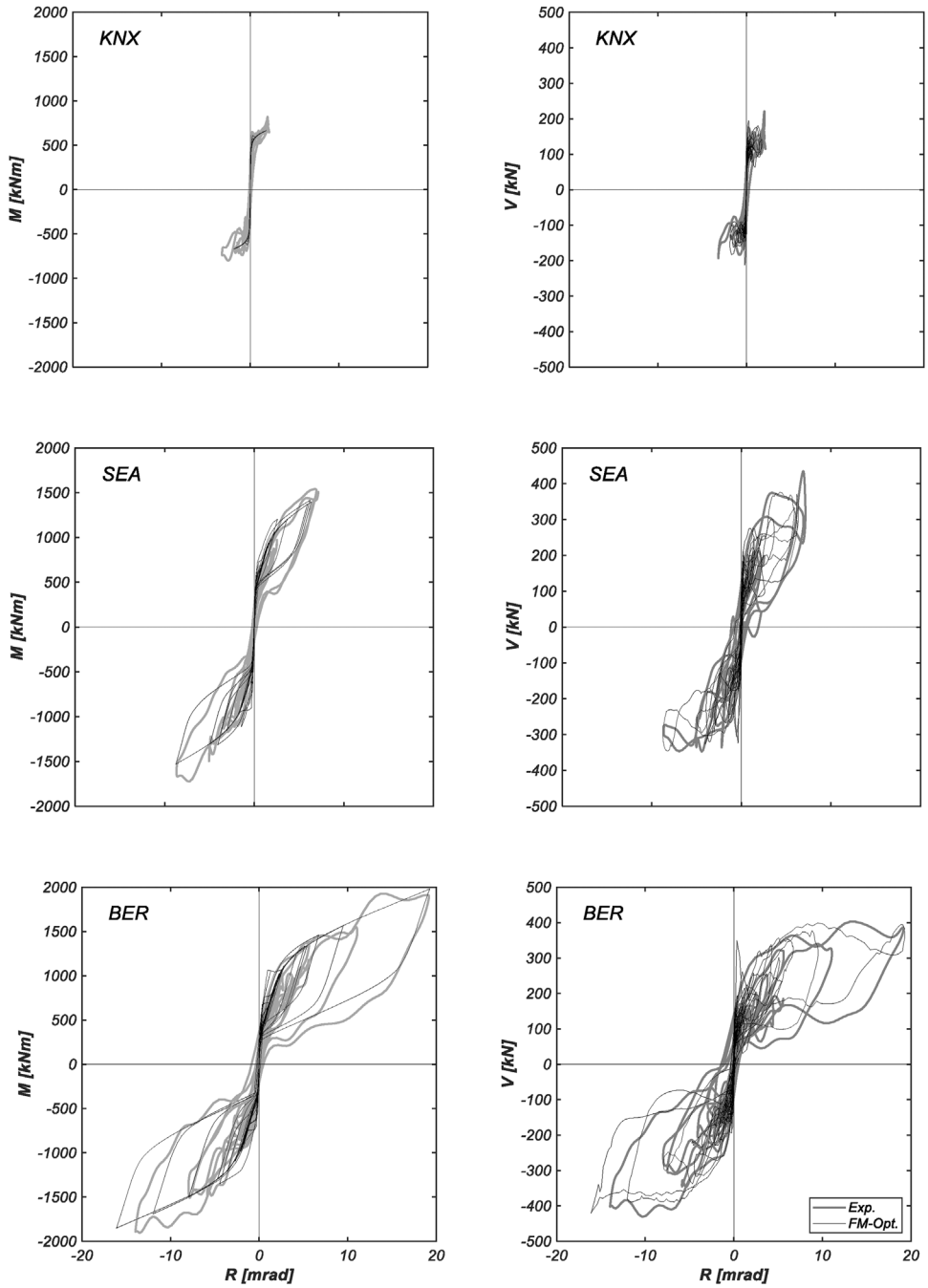

FIGURE 11 | Time history results (FM) for Knoxville, Seattle-4 and Berkeley-DBE in terms of base moment–base rotation (left side) and base shear–base rotation (right side).

Note: In grey line the experimental test and in black line the numerical results.

performed. Building on the single-wall analyses presented in the previous section, the modelling framework was extended to the system level, where interactions among walls, floor diaphragms, and columns influence the global response. Accordingly, this section presents the finite element models for the complete three-storey precast test structure, directly incorporating the calibrated wall formulations. A constrained least-squares optimisation procedure is then applied to refine the governing parameters at the system level and improve the simulation of the building's nonlinear dynamic response.

The finite element modelling strategies previously described for the walls were directly applied to the modelling of the entire structure (Figure 10). Additional details on the finite element implementation are provided in the Supplementary Material, while geometric and mechanical properties were taken from Schoettler et al. [11]. In the global model, the columns were represented by elastic beam elements in their actual positions. The bending capacity of the column–foundation connections was modelled using zero-length elements with nonlinear moment–rotation hysteresis [11]. Each floor diaphragm was modelled as

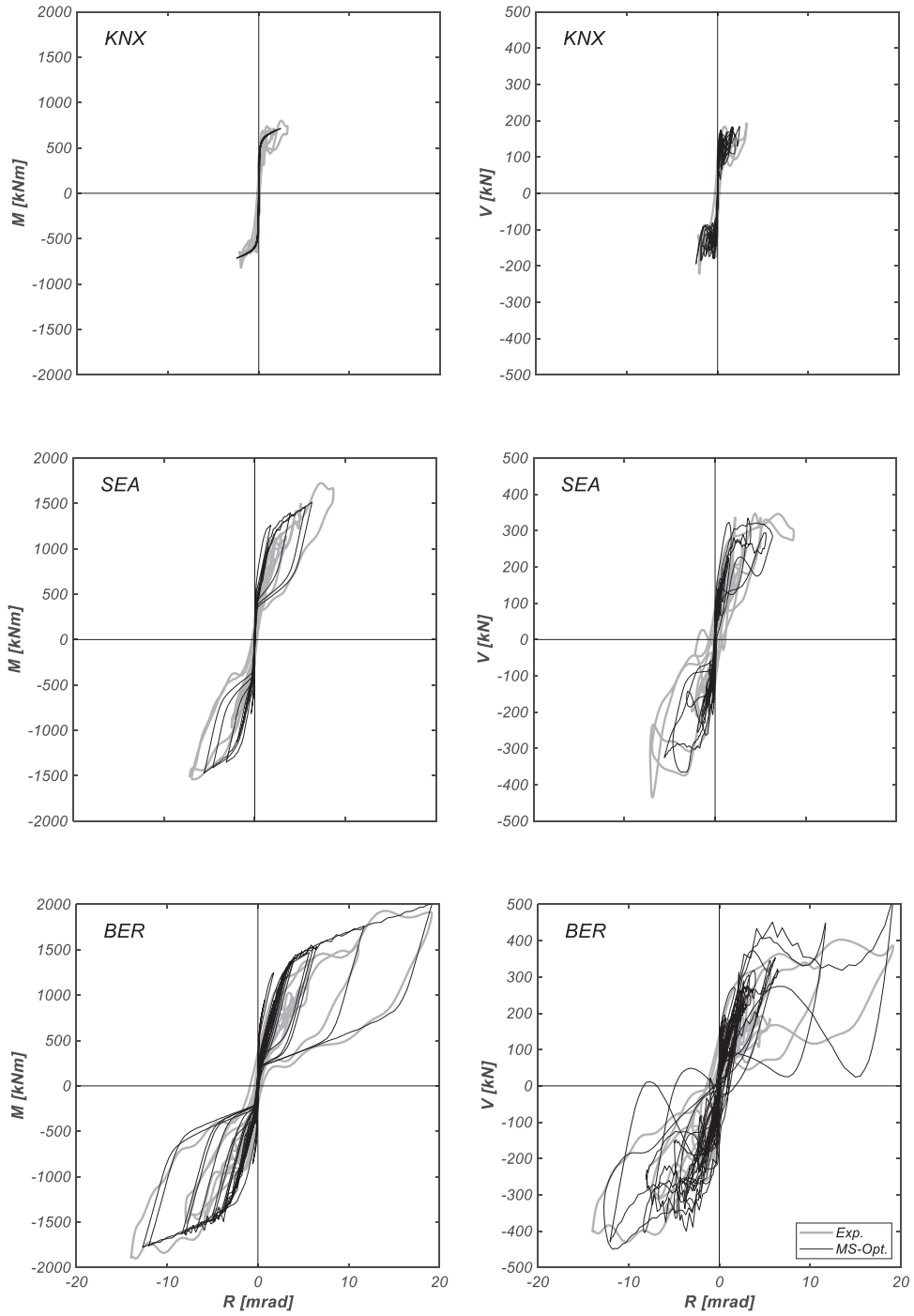

FIGURE 12 | Time history graphs (MS model) for Knoxville, Seattle-4 and Berkeley-DBE in terms of base moment–base rotation (left side) and base shear–base rotation (right side).

Note: In grey line the experimental test and in black line the numerical results.

a beam-like element, and all structural elements included shear deformations (Timoshenko formulation). Rigid links ensured compatibility between columns and floor nodes, and floor masses were lumped at diaphragm and column nodes. The wall-diaphragm connections are slotted along the vertical direction [11, 32], meaning that only horizontal forces can be transmitted. Accordingly, vertical and in-plane rotational releases were introduced in the FE model at these connections.

As the present study focuses on the accurate modelling of rocking walls, the floor diaphragms were represented as elastic elements with reduced in-plane stiffness, without explicitly modelling the connections between adjacent floor units. This simplified approach reproduces the experimental response while limiting modelling complexity. The stiffness reduction adopted for each floor diaphragm was calibrated following Schoettler [53]. Calibration was performed through dynamic analyses of

TABLE 4 | Best parameter values resulting from the optimisation process (RS model).

	R_1 (mrad)	M_1 (kNm)	R_2 (mrad)	M_2 (kNm)	$K_{R,0}$ (kNm/mrad)	$K_{R,f}$ (kNm/mrad)
Ref. Values—rocking wall (KNX)	0.154	610	20	1900	3961	65
Ref. Values—hybrid wall (SEA-4, BER)	0.620	950	35	2000	1532	31
KNX	4.85·R_1	0.65·M_1	R_2	4.00·M_2	531	374
SEA-4	1.30·R_1	0.50·M_1	R_2	2.50·M_2	589	132
BER	1.50·R_1	0.63·M_1	R_2	1.30·M_2	644	59

Note: $K_{R,0}$ is the initial rotational stiffness; $K_{R,f}$ is the tangent rotational stiffness during rocking.

the complete structural model by comparing relative floor–wall accelerations in the frequency domain. Good agreement between numerical and experimental results was achieved, confirming the adequacy of the adopted modelling strategy. Detailed Fourier spectra and calibrated stiffness values are provided in the Supplementary Material.

5.1 | Numerical Optimisation

An optimisation procedure was implemented to calibrate the numerical models and ensure that their simulated response consistently reproduces the experimentally observed behaviour. Given the number of parameters governing the nonlinear dynamic response and their interaction effects, a global optimisation framework was adopted. This allows simultaneous variation of key parameters, avoiding record-specific overfitting and providing physically meaningful parameter sets across different seismic inputs. Accordingly, a constrained nonlinear least-squares optimisation problem was formulated and solved using the built-in *lsqnonlin* function in MATLAB [54]:

$$[x, obj] = lsqnonlin\,(fun, x_0, l_b, u_b, options) \tag{8}$$

In the above expression, x_0 is the starting value of the considered parameters, l_b and u_b are the lower and upper bounds on the parameters, respectively, *fun* is the objective function that should be minimised based on the results of the finite element numerical model, x is the final value obtained from the optimisation process and *obj* is the corresponding value of the objective function. The objective function was defined based on the maximum displacement at the top of the wall D_{top} and of the maximum base shear V_{base}. To avoid spurious effects associated with gap closure, base shear was evaluated considering the open-gap configuration [32]. The value of the objective function results from the sum of the residuals with respect to D_{top} and V_{base} from the experimental test ('Test') and the numerical model ('FE').

$$fun = \frac{\left|\max\left(\left|D_{top}\right|\right)_{Test} - \max\left(\left|D_{top}\right|\right)_{FE}\right|}{\max\left(\left|D_{top}\right|\right)_{Test}} + \frac{\left|\max\left(|V_{base}|\right)_{Test} - \max\left(\left|V_{base}\right|\right)_{FE}\right|}{\max\left(\left|V_{base}\right|\right)_{Test}} \tag{9}$$

A multistart approach was adopted to improve convergence towards the global minimum. In the FM model, the optimisation variables were $E_{rocking}$, the damping ratio (ξ) and the strain penetration length (L_s), while for the MS model the parameters were the axial stiffness of the translational springs at the base ($K_{spring} = E_c A / L_{wall}$), L_s and ξ.

Table 3 presents the optimal parameter values obtained for the FM and MS models. For the FM model, the optimisation yields consistent values across all ground motions, closely matching the analytical estimates ($L_s = 12\phi$ and $E_{\text{rocking}} \approx 0.015\,E_c$). Additional analyses performed using both analytical and optimised parameters show negligible discrepancies (within 4%), confirming the validity of the proposed formulation. For the MS model, the analytical estimate corresponds to about 1.45 K_{spring} (i.e., $L_{\text{spring}} \approx 0.69\,L_w$). While good agreement is obtained for the KNX record, lower stiffness values are identified for SEA-4 and BER. This is compensated by increased damping and reduced L_s, indicating interaction among parameters in reproducing the global response. It is important to note that the optimised value $L_s = 6\phi$ should be interpreted as an equivalent modelling parameter, rather than as a direct physical estimate of the actual strain penetration length. Additional analyses using analytically derived parameters show discrepancies below 6%, indicating that the analytical formulation provides a mechanically consistent approximation of the interface behaviour.

The optimised parameters were adopted for subsequent analyses, showing generally good agreement with the experimental response (Figure 11, Figure 12).

The rotational spring (RS) formulation was also examined. In this approach, the rocking behaviour is represented by a bilinear moment–rotation relationship at the wall base [7, 32]. The key parameters defining this relationship are the bending moments M_i and corresponding rotations R_i associated with the characteristic points of the bilinear curve. For the hybrid wall configuration, an additional rotational component accounts for energy dissipation. In this case, the parameters M_i and R_i reported in Table 4 refer exclusively to the rocking component, while the contribution of the dissipative bars was introduced through a fixed additional moment capacity $\Delta M = 526$ kNm. The optimisation procedure was performed considering M_1, R_1 and M_2 as free parameters, while the remaining parameters were kept constant.

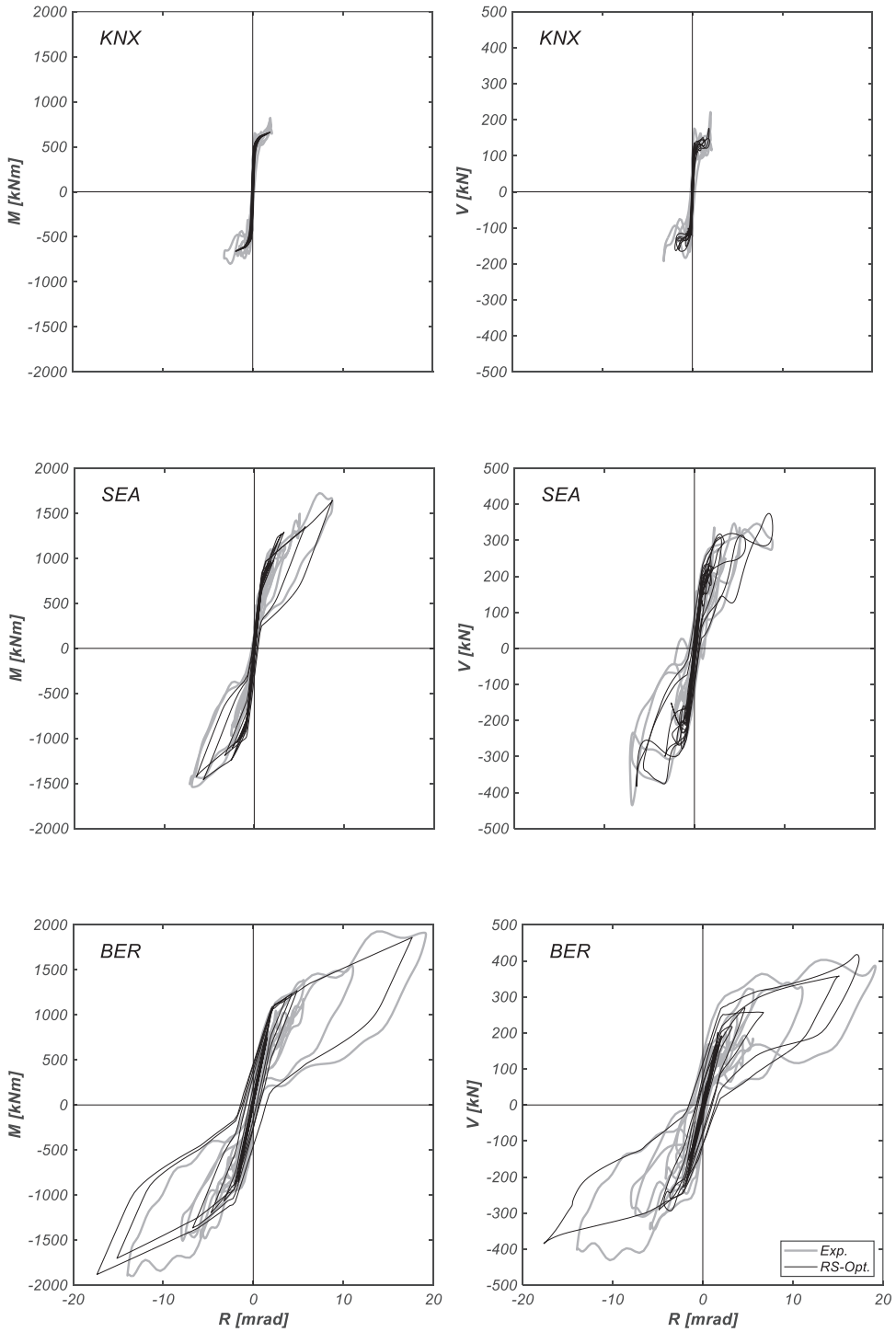

FIGURE 13 | Time history graphs (RS model) for Knoxville, Seattle-4 and Berkeley-DBE in terms of base moment–base rotation (left side) and base shear–base rotation (right side).

Note: In grey line the experimental test and in black line the numerical results.

Table 4 shows a consistent trend in the optimised parameters across all seismic inputs: the initial rotational stiffness is substantially reduced compared to the reference values, while the tangent stiffness during rocking increases. This redistribution indicates that the original bilinear formulation overestimates initial stiffness and underestimates stiffness at larger rotations. Notably, the resulting initial stiffness is similar under all conditions, both rocking and hybrid, and across all intensities. This finding aligns with the analytical results presented in the previous section. From the analytical formulation presented in Section 4, it is possible to estimate the initial rotational stiffness $K_{R,0}$ by directly multiplying the axial stiffness in Equation 6 by the square of the neutral axis

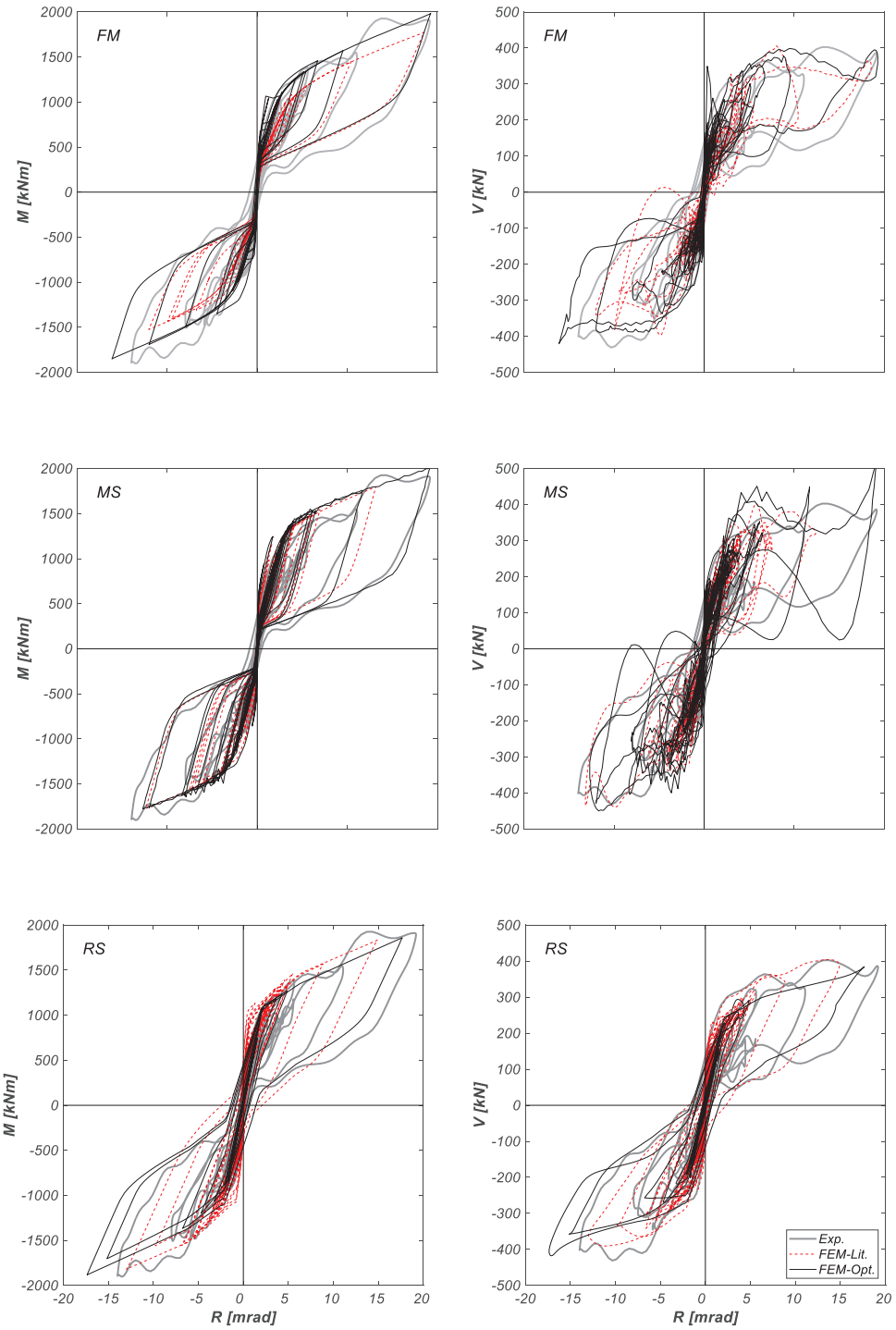

FIGURE 14 | Time history graphs for Berkeley-DBE in terms of wall base moment and base shear.

Note: In the grey line the experimental results, in the red line the numerical results with the parameters from the literature and in the black line the numerical results after the optimisation process.

depth:

$$K_{R,0} = k_{eq} \cdot (\chi \cdot L_w)^2 = \frac{5}{9} E_c t \frac{\chi^3}{\chi + 1} {L_w}^2 \tag{10}$$

Assuming a neutral axis depth at incipient rocking equal to 30% of the wall depth ($\chi = 0.30$), $K_{R,0}$ is 500 kNm/mrad, consistent with the optimisation results. Despite this agreement, the RS model achieves accuracy through redistribution among a limited number of lumped parameters, indicating reduced parameter transferability. While computationally efficient, this suggests that the RS formulation is more suitable for preliminary analyses than for detailed calibration. The optimised parameters were subsequently used in the nonlinear dynamic analyses presented in Figure 13.

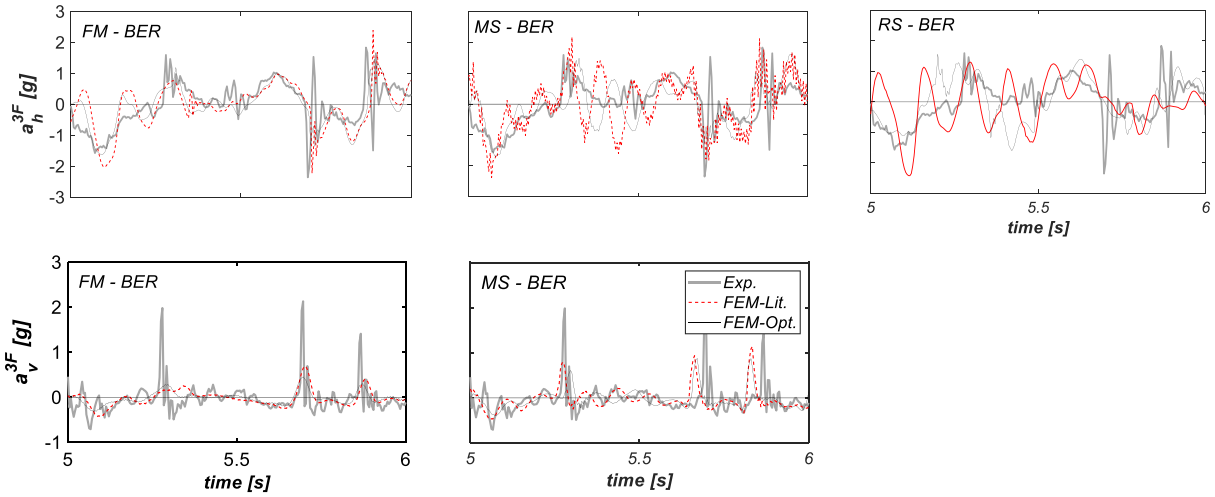

FIGURE 15 | Time history graphs in terms of wall horizontal (top row) and vertical (bottom row) accelerations at the third level for the FM, MS and RS models for Berkeley-DBE.

Note: In the grey line the experimental results, in the red line the numerical results with the parameters from the literature and in the black line the numerical results after the optimisation process.

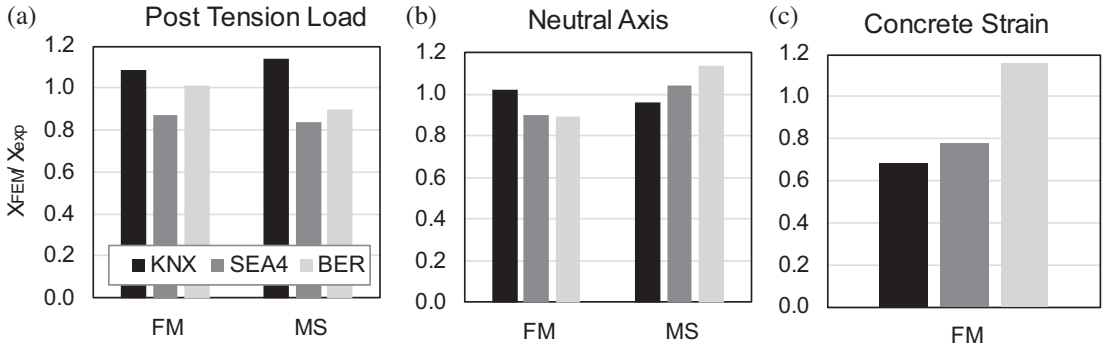

FIGURE 16 | Comparison of local responses: (a) average post-tensioning force in the steel tendons; (b) neutral axis depth at the wall base; (c) average concrete compressive strain at the east and west wall toes. Numerical results are normalised with respect to the corresponding experimental measurements. Results obtained using the fibre-based (FM) and multi-spring (MS) formulations are reported.

5.2 | Discussion and Comparison of the Results Before and After Optimisation

Figure 14 compares the numerical responses obtained using reference parameter values from the literature and the optimised parameter sets with the experimental measurements. A significant improvement in the simulation of the global response is observed after optimisation, particularly for the FM and MS models. For the BER ground motion, which represents the most demanding case, the relative error in peak base rotation is reduced from 4.1% to 0.4% for the FM model, from 30.5% to 0.3% for the MS model, and from 22.5% to 7.9% for the RS model. Similar reductions are observed for peak base shear and base moment for the KNX and SEA-4 ground motions.

Figure 15 shows the horizontal and vertical accelerations at the third floor for the BER ground motion. The MS model exhibits the greatest improvement in reproducing acceleration peaks associated with gap closure. Although optimisation improves the overall response, some discrepancies remain, particularly in the later stages of the records, likely due to higher-mode effects not fully captured by the simplified models.

Local response quantities are compared in Figure 16, including post-tensioning forces, neutral axis depth and concrete compressive strain. Numerical results are normalised with respect to the corresponding experimental measurements. Both FM and MS models show good agreement with experimental results for post-tensioning forces and neutral axis depth, with slightly larger discrepancies observed for local strain measures. Concrete strain is reliably captured only by the FM model, which reproduces overall trends despite some under- and over-estimation depending on the ground motion intensity.

The optimisation results provide further insight into the behaviour of the different modelling approaches. The FM model yields consistent parameter values across all ground motions, confirming the validity of the analytical formulation. The MS model identifies parameter combinations that compensate for

each other, allowing accurate reproduction of the global response despite variability in individual parameters.

The RS formulation offers computational simplicity but shows higher sensitivity to the selected ground motion, resulting in reduced robustness compared to the FM and MS models.

Overall, all modelling approaches benefit from optimisation, but clear differences emerge in robustness and transferability. The FM model provides the most consistent performance across different conditions, accurately reproducing both global and local responses. The MS model offers a physically meaningful representation of distributed contact behaviour and improves the simulation of acceleration peaks. The RS model, while efficient, is more suitable for preliminary analyses due to its sensitivity to calibration.

6 | Conclusions

This paper examined the finite element modelling of rocking and hybrid precast concrete walls through a systematic comparison of three alternative modelling strategies: a fibre-based formulation, a distributed compression-only translational spring model and a lumped rotational spring model. The approaches were investigated at both the component and system levels and validated against shake-table tests conducted on a three-storey, half-scale precast concrete building representative of a parking structure, tested at the University of California, San Diego. Based on the results of this study, the following conclusions can be drawn:

i. The response of rocking and hybrid walls is governed by a limited number of parameters, primarily related to wall–foundation interface deformability, strain penetration of the dissipative bars and damping representation

ii. An analytical formulation was developed to obtain mechanically consistent estimates of the interface-related parameters, and its outputs were validated through global optimisation against experimental results.

iii. A small mass-proportional viscous damping ratio was introduced to account for energy dissipation mechanisms not explicitly captured by the models, including gap closure, interface friction and impact-related losses.

iv. The fibre-based model demonstrated the most robust performance, reproducing both global and local response quantities, including post-tensioning forces, neutral axis depth and concrete compressive strains, with optimised parameters that remained largely transferable across different ground motions.

v. The distributed spring model improved the simulation of acceleration peaks associated with gap closure but showed greater parameter sensitivity to seismic input, limiting transferability.

vi. The rotational spring model was the most computationally efficient (approximately one-third the cost of the other approaches) but is better suited to preliminary analyses or parametric screening than simulating detailed responses. From a computational standpoint, the fibre model offers the best accuracy-to-computation-time ratio, particularly for high-intensity events, where it also outperforms the MS model in efficiency.

vii. The three modelling strategies represent a practical spectrum of options, and the results provide quantitative guidance for selecting and calibrating finite element models for rocking and hybrid precast walls.

Acknowledgments

Open access publishing facilitated by Universita degli Studi di Bergamo, as part of the Wiley - CRUI-CARE agreement.

Data Availability Statement

The data that support the findings of this study are available in Data Center Hub at https://datacenterhub.org/post-nees.html, reference number 450. These data were derived from the following resources available in the public domain: NEES-2005-0046, https://datacenterhub.org/landingpages/450/450_LandingPage.html

References

1. L. G. Cormack, "The Design and Construction of the Major Bridges on the Mangaweka Rail Deviation," *Transactions of the Institute of Professional Engineers of New Zealand* 15 (1998): 6–23.

2. Y. C. Kurama, R. Sause, S. Pessiki, and L.-W. Lu, "Lateral Load Behavior and Seismic Design of Unbonded Posttensioned Precast Concrete Walls," *ACI Structural Journal* 96, no. 4 (1999): 622–632, https://doi.org/10.14359/700.

3. Y. C. Kurama, S. Pessiki, R. Sause, and L.-W. Lu, "Seismic Behavior and Design of Unbonded Posttensioned Precast Concrete Walls," *PCI Journal* 44, no. 3 (1999): 72–89, https://doi.org/10.15554/pcij.05011999.72.89.

4. Y. C. Kurama, "Seismic Design of Partially Post-Tensioned Precast Concrete Walls," *PCI Journal* 50, no. 4 (2005): 100–125, https://doi.org/10.15554/pcij.07012005.100.125.

5. Y. C. Kurama, "Seismic Design of Unbonded Post-Tensioned Precast Walls With Supple-Mental Viscous Damping," *ACI Structural Journal* 97, no. 4 (2000): 648–658.

6. M. J. N. Priestley, S. Sritharan, J. R. Conley, and S. Pampanin, "Preliminary Results and Conclusions From The Presss Five-Story Precast Concrete Test Building," *PCI J* 44, no. 6 (1999): 42–67, https://doi.org/10.15554/PCIJ.11011999.42.67.

7. J. I. Restrepo and A. Rahman, "Seismic Performance of Self-Centering Structural Walls Incorporating Energy Dissipators," *Journal of Structural Engineering* 133, no. 11 (2007): 1560–1570, https://doi.org/10.1061/(ASCE)0733-9445(2007)133:11(1560).

8. T. Holden, J. Restrepo, and J. B. Mander, "Seismic Performance of Precast Reinforced and Prestressed Concrete Walls," *Journal of Structural Engineering* (2003): 286–296, https://doi.org/10.1061/(ASCE)0733-9445(2003)129:3(286).

9. Q. T. Ma and M. H. Khan, "Free Vibration Tests of a Scale Model of the South Rangitikei Rail-Way Bridge," in *Proceedings of the New Zealand Society for Earthquake Engineering (NZSEE) Conference* (2008).

10. Q. T. Ma and M. H. Khan, "Shake Table Tests of a Stepping Bridge Model," in *14th World Conference on Earthquake Engineering* (International Association for Earthquake Engineering, 2008).

11. M. Schoettler, A. Belleri, D. Zhang, J. I. Restrepo, and R. B. Fleischman, "Preliminary Results of the Shake-Table Testing For The Development of a Diaphragm Seismic Design Methodology," *PCI Journal* (2009): 100–124, https://doi.org/10.15554/pcij.01012009.100.124.

12. G. Tsampras, R. Sause, R. B. Fleischman, J. I. Restrepo, A. Nema, and Z. Zhang, "Practical Force-Limiting Deformable Connections in Buildings With Rocking Base Mechanism and Limited Higher-Mode Responses," in P*roceedings of the 12th National Conference on Earthquake Engineering* (EERI, 2022).

13. A. M. Rahman and J. I. Restrepo-Posada, "Earthquake Resistant Precast Concrete Buildings: Seismic Performance of Cantilever Walls Prestressed Using Unbonded Tendons," Research Report No. 200-5 (Department of Civil Engineering, University of Canterbury, 2000).

14. T. Koshikawa, "Moment and Energy Dissipation Capacities of Post-Tensioned Precast Concrete Connections Employing a Friction Device," *Engineering Structures* 138 (2017): 170–180, https://doi.org/10.1016/J.ENGSTRUCT.2017.02.012.

15. D. Marriott, S. Pampanin, D. Bull, and A. Palermo, "Dynamic Testing of Precast, Post-Tensioned Rocking Wall Systems With Alternative Dissipating Solutions," *Bulletin of the New Zealand Society for Earthquake Engineering* 41, no. 2 (2008): 90–103, https://doi.org/10.5459/BNZSEE.41.2.90-103.

16. G. W. Rodgers, K. M. Solberg, J. B. Mander, J. G. Chase, B. A. Bradley, and R. P. Dhakal, "High-Force-to-Volume Seismic Dissipators Embedded in a Jointed Precast Concrete Frame," *Journal of Structural Engineering* 138, no. 3 (2010): 375–386, https://doi.org/10.1061/(ASCE)ST.1943-541X.0000329.

17. G. W. Rodgers, K. M. Solberg, J. G. Chase, et al., "Performance of a Damage-Protected Beam–Column Subassembly Utilizing External Hf2v Energy Dissipation Devices," *Earthquake Engineering and Structural Dynamics* 37, no. 13 (2008): 1549–1564, https://doi.org/10.1002/eqe.830.

18. V. Mpampatsikos, M. E. Bressanelli, A. Belleri, and R. Nascimbene, "A Non-Dimensional Parametric Approach for the Design of Pt Tendons and Mild Steel Dissipaters In Precast Rocking Walls," *Engineering Structures* (2020): 110513, https://doi.org/10.1016/j.engstruct.2020.110513.

19. J. Conley, S. Sritharan, and M. J. N. Priestley, "Precast seismic Structural Systems PRESSS-3: The Five-Story Precast Test Building, Vol. 3-1: Wall Direction Response," Report No. SSRP-99/19 (La Jolla, University of California, San Diego, 2002).

20. M. J. N. Priestley, G. M. Calvi, and M. J. Kowalsky, *Displacement-Based Seismic Design of Structures* (Istituto Universitario di Studi Superiori di Pavia, 2007).

21. M. J. N. Priestley and J. R. T. Tao, "Seismic Response of Precast Prestressed Concrete Frames With Partially Debonded Tendons," *PCI Journal* 38, no. 1 (1993): 58–69, https://doi.org/10.15554/PCIJ.01011993.58.69.

22. A. Belleri, M. Torquati, and P. Riva, "Finite Element Modeling of "Rocking Walls"," in *4th ECCOMAS Thematic Conference on Computational Methods in Structural Dynamics and Earthquake Engineering* (2013), https://doi.org/10.7712/120113.4706.C1213.

23. S. Gavridou, J. W. Wallace, T. Nagae, T. Matsumori, K. Tahara, and K. Fukuyama, "Shake-Table Test of a Full-Scale 4-Story Precast Concrete Building. i: Overview and Experimental Results," *Journal of Structural Engineering* 143, no. 6 (2017): e04017033, https://doi.org/10.1061/(ASCE)ST.1943-541X.0001756.

24. D. Kalliontzis and M. Nazari, "Unbonded Post-Tensioned Precast Concrete Walls With Rocking Connections: Modeling Approaches and Impact Damping," *Frontiers in Built Environment* 7 (2021): 638509, https://doi.org/10.3389/fbuil.2021.638509.

25. Y. Liu and W. Zhou, "Numerical Modeling to Predict Seismic Performance of the Post-Tensioned Self-Centering Concrete Shear Walls," *Bulletin of Earthquake Engineering* 7 (2021): 7–25, https://doi.org/10.1007/s10518-021-01309-4.

26. M. Nazari, "Seismic Performance of Unbonded Post-Tensioned Precast Wall Systems Subjected to Shake Table Testing," (PhD diss., Department of Civil, Construction and Environmental Engineering, Iowa State University, 2016), https://doi.org/10.31274/ETD-180810-4850.

27. K. M. Twigden and R. S. Henry, "Shake Table Testing of Unbonded Post-Tensioned Concrete Walls With and Without Additional Energy Dissipation," *Soil Dynamics and Earthquake Engineering* 119 (2018): 375–389, https://doi.org/10.1016/j.soildyn.2018.05.007.

28. M. E. Bressanelli, A. Belleri, and J. I. Restrepo, "Finite Element Modelling of a RC Rocking Wall With Additional Steel Rebars," in Proceedings of the 8th International Conference on Computational Methods in Structural Dynamics and Earthquake Engineering (COMPDYN 2021) (National Technical University of Athens, 2021), https://doi.org/10.7712/120121.8591.19206.

29. A. Nema, *Development of Low Seismic Damage Structural Systems. A dissertation submitted in partial satisfaction of the requirements for the degree of Doctor of Philosophy in Structural Engineering* (University of California, 2018).

30. G. Guerrini, J. I. Restrepo, A. Vervelidis, and M. Massari, *Self-Centering Precast Concrete Dual-Steel-Shell Columns for Accelerated Bridge Construction: Seismic Performance, Analysis* (Pacific Earthquake Engineering Research Center, 2015).

31. A. Palermo, S. Pampanin, and D. Marriott, "Design, Modeling, and Experimental Response of Seismic Resistant Bridge Piers With Post-tensioned Dissipating Connections," *Journal of Structural Engineering, American Society of Civil Engineers* 133, no. 11 (2007): 1648–1661, https://doi.org/10.1061/(ASCE)0733-9445.

32. A. Belleri, M. J. Schoettler, J. I. Restrepo, and R. B. Fleischman, "Dynamic Behavior of Rocking and Hybrid Cantilever Walls in a Precast Concrete Building," *ACI Structural Journal* 111, no. 3 (2014): 661–671, https://doi.org/10.14359/51686778.

33. R. B. Fleischman, C. Naito, J. Restrepo, et al., "Precast Diaphragm Seismic Design Methodology (DSDM) Project, Part 2: Research Program," *PCI Journal* 50, no. 6 (2005): 14–31, https://doi.org/10.15554/pcij.11012005.14.31.

34. J. I. Restrepo, J. P. Conte, J. E. Luco, F. Seible, and L. Van Den Einde, "The NEES@ UCSD large high performance outdoor shake table," in Proceedings of the Structures Congress 2005 (American Society of Civil Engineers, 2005), 1–16, https://doi.org/10.1061/40779(158)1.

35. L. Van Den Einde, J. Restrepo, and J. P. Conte, "Development of the George E. Brown Jr. Network For Earthquake Engineering Simulation (NEES) Large High Performance Outdoor Shake Table at the University of California, San Diego," in *Proceedings of the 13th World Conference on Earthquake Engineering* (2004).

36. F. McKenna, G. Fenves, and M. Scott, *Open System for Earthquake Engineering Simulation (OpenSees): User Command-Language Manual* (University of California, 2000).

37. A. Belleri, B. Moaveni, and J. I. Restrepo, "Damage Assessment Through Structural Identification of a Three-Story Large-Scale Precast Concrete Structure," *Earthquake Engineering Structural Dynamics* 43 (2014): 61–76, https://doi.org/10.1002/eqe.2332.

38. J. B. Mander, M. J. N. Priestley, and R. Park, "Theoretical Stress-Strain Model for Confined Concrete," *Journal of Structural Engineering* 114, no. 8 (1988): 1804–1826, https://doi.org/10.1061/(ASCE)0733-9445(1988)114:8(1804).

39. A. Vulcano and V. V. Bertero, "Analytical Models for Predicting the Lateral Response of RC Shear Walls: Evaluation of Their Reliability," Report No. UCB/EERC-87/19 (Earthquake Engineering Research Center, University of California, 1987).

40. L. L. Dodd and J. I. Restrepo-Posada, "Model for Predicting Cyclic Behavior of Reinforcing Steel," *Journal of Structural Engineering* 121, no. 3 (1995): 433–445, https://doi.org/10.1061/(ASCE)0733-9445(1995)121:3(433).

41. M. Nazari, S. Sritharan, and S. Aaleti, "Single Precast Concrete Rocking Walls as Earthquake Force resisting elements," *Earthquake Engineering and Structural Dynamics* 46, no. 5 (2007): 753–769, https://doi.org/10.1002/EQE.2829.

42. G. Taylor, "The Nonlinear Seismic Response of Tall Shear Wall Structures," (PhD diss., University of Canterbury, University of Canterbury, 1977).

43. W. D. Trono, "Earthquake Resilient Bridge Columns Utilizing Damage Resistant Hybrid Fiber reinforced Concrete," (PhD diss., University of California, 2014).

44. H. A. Spieth, A. J. Carr, A. G. Murahidy, D. Arnolds, M. Davies, and J. B. Mander, *Modelling of Post-Tensioned Precast Reinforced Concrete Frame Structures With Rocking Beam-Column Connections* (Department of Civil Engineering, University of Canterbury, 2004).

45. F. A. Charney, "Unintended Consequences of Modeling Damping in Structures," *ASCE Journal of Structural Engineering* 134, no. 4 (2008): 581–592, https://doi.org/10.1061/(ASCE)0733-9445(2008)134:4(581).

46. J. F. Hall, "Problems Encountered From the Use (or misuse) of Rayleigh Damping," *Earthquake Engineering and Structural Dynamics* 35 (2006): 525–545, https://doi.org/10.1002/eqe.541.

47. L. Petrini, C. Maggi, M. J. Priestley, and G. M. Calvi, "Experimental Verification of Viscous Damping Modeling for Inelastic Time History Analyzes," *Journal of Earthquake Engineering* 12, no. S1 (2008): 125–145, https://doi.org/10.1080/13632460801925822.

48. G. Gazetas and N. Makris, "Dynamic Pile-Soil-Pile Interaction. Part I: Analysis of Axial Vibration," *Earthquake Engineering & Structural Dynamics* 20, no. 2 (1991): 115–132, https://doi.org/10.1002/eqe.4290200203.

49. N. Makris and G. Gazetas, "Displacement Phase Differences in a Harmonically Oscillating Pile," *Geotechnique* 43, no. 1 (1993): 135–150, https://doi.org/10.1680/geot.1993.43.1.135.

50. Y. Shayah, "Soil Structure Interaction and the Radiation Damping: A State-of-the-Art Review," *Results in Engineering* 26 (2025): 104755, https://doi.org/10.1016/j.rineng.2025.104755.

51. J. P. Wolf, *Dynamic Soil-Structure Interaction* (Prentice Hall, 1985).

52. L. Wiebe and C. Christopoulos, "Characterizing Acceleration Spikes Due to Stiffness Changes in Nonlinear Systems," *Earthquake Engineering and Structural Dynamics* 39 (2010): 1653–1670, https://doi.org/10.1002/eqe.1009.

53. M. J. Schoettler, "*Seismic Demands in Precast Concrete Diaphragms*," (PhD diss., University of California, 2010).

54. The MathWorks, Inc. 2021. *MATLAB R2021*. The MathWorks, Inc.

55. MIDAS Information Technology Co., Ltd. 2025. Midas Gen 2025 (Version 2.1). MIDAS Information Technologies Co. Ltd.

Supporting Information

Additional supporting information can be found online in the Supporting Information section.

Supporting File 1: eqe70173-sup-0001-SuppMat.pdf.

Appendix

This appendix provides additional support to the analytical formulation presented in Section 4. An elastic two-dimensional model of the wall was developed using quadrilateral finite elements in MidasGEN [55]. The wall was subjected to a triangular lateral load combined with axial post-tensioning and compression-only boundary conditions at the base, to reproduce the rocking mechanism (Figure A1).

The stress distribution was extracted along horizontal sections at different elevations, ranging from 0 to 2.8 m at 0.4 m intervals. The coordinates of the intersections with the zero-stress line, which define the neutral axis depth at each elevation, are plotted in Figure A2 as a function of wall height and compared with the analytical prediction. A good agreement is observed between the numerical results and the simplified formulation.

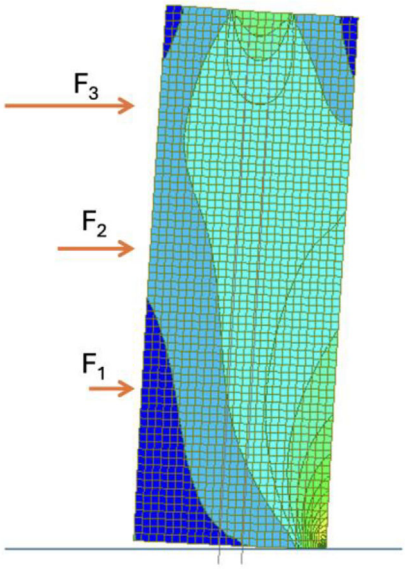

FIGURE A1 | Considered finite element model used to investigate the wall deformations at the base during rocking. The contour lines represent the normal stress along the vertical direction.

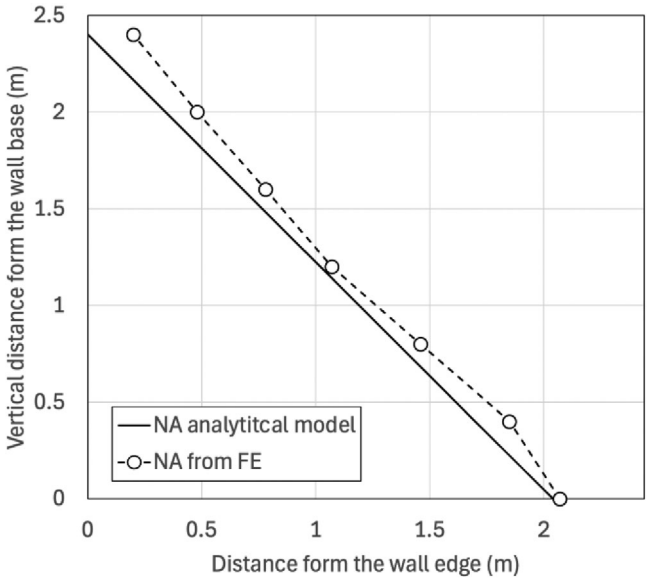

FIGURE A2 | Neutral axis depth along cutting lines at different wall elevations in terms of vertical normal stresses. The corresponding idealised linear compressive stress distributions are also shown in red dashed lines, with the intersection with the zero-stress line indicating the neutral axis depth at each elevation associated with this distribution.

The corresponding stress profiles are shown in Figure A3, together with the idealised linear distributions in the compressed region.

The coordinates of these intersection points are plotted in Figure A3 as a function of wall height and compared with the analytical prediction. A good agreement is observed between numerical results and the simplified formulation.

These results confirm the validity of the assumed linear variation of the compressed zone along the wall height and support the analytical expressions adopted in the main text.

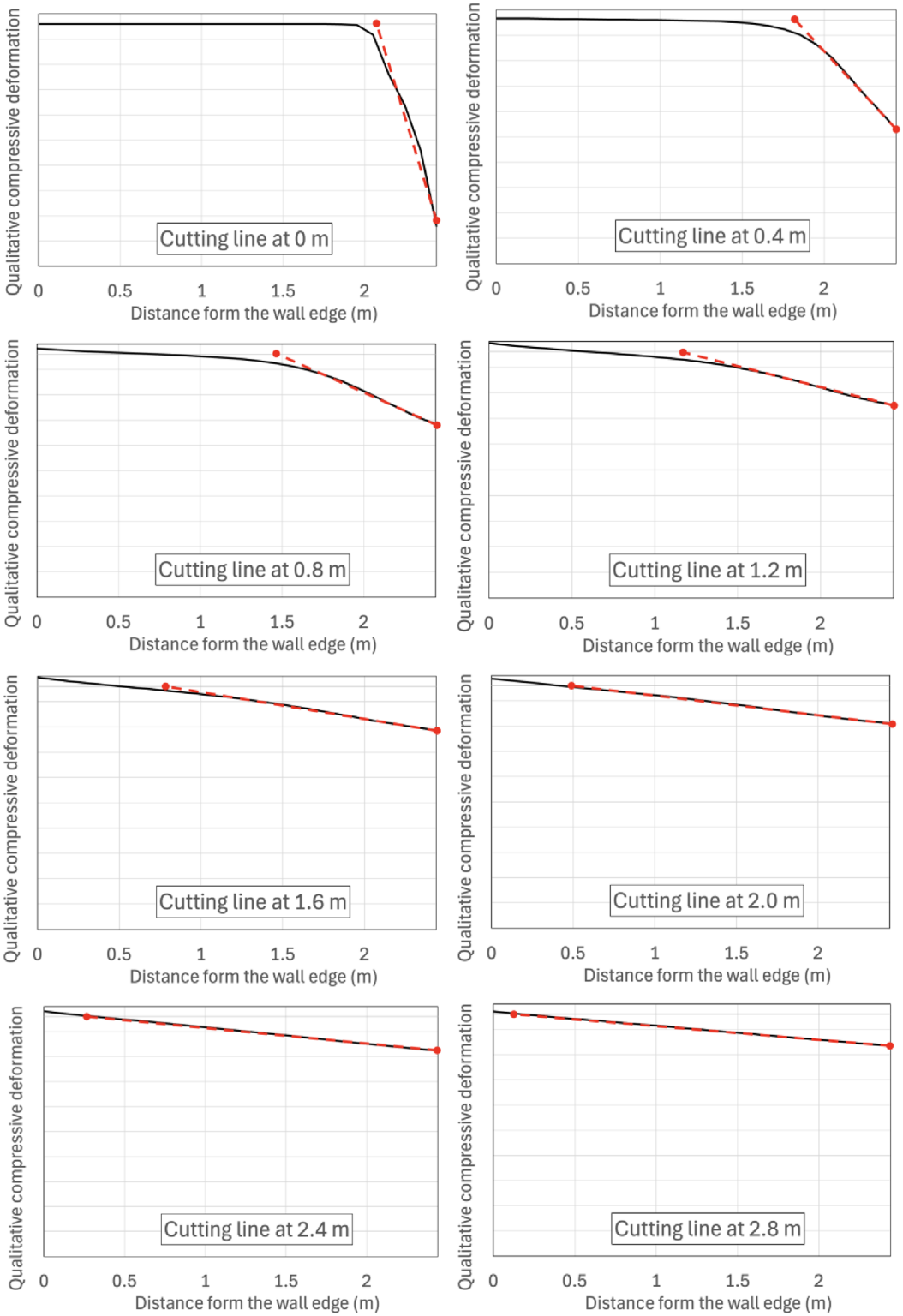

FIGURE A3 | Neutral axis depth along the wall height derived from the finite element results compared with the simplified analytical prediction.